# APPENDIX 1

(Lituiev et al. 2013, Development 140)

## *SUPPLEMENTARY TEXT*

### *Simulation conditions and parameter values*

The reaction-diffusion model described in the main text was studied in the form of a partial differential equation with boundary conditions:

$$\frac{\partial u}{\partial t} = D \cdot \nabla^2 u - \hat{a} \cdot u + \hat{b}$$

$$\nabla u|_{\Gamma_1} = -\hat{p}$$

$$\nabla u|_{\Gamma_2} = -\hat{q} \cdot u$$

Where $u$ is the auxin concentration, $D$ is the diffusion coefficient, $\hat{a}$ is the degradation rate, $\hat{b}$ is the synthesis rate, $\hat{p}$ is the influx rate, and $\hat{q}$ is efflux rate, $\Gamma_1$ is the boundary domain of influx (micropyle, $x = 0$ in one dimension) and $\Gamma_2$ is the boundary domain of efflux (chalaza, $x = 1$ in one dimension). The $\nabla$ sign represents the gradient operation (first spatial derivative), and $\nabla^2$ is the Laplacian operator (second spatial derivative). The equation thus describes the local instanteneous change of the auxin concentration, which is influenced by the diffusion ($D \cdot \nabla^2 u$ term), degradation (-$\hat{a}\,u$), and synthesis ($\hat{b}$).

Further, we rescale the degradation rate and the efflux rate by the length ($L$) of the female gametophyte (FG) and diffusion rate ($D$); the rescaled degradation rate becomes $a = \hat{a} \cdot \frac{L^2}{D}$ and the rescaled efflux rate $q = \hat{q} \cdot \frac{L}{D}$. As the differential equation is linear, the influx rate and synthesis rate can be selected arbitrary. We chose these parameters such to equal the mean concentration of auxin with the value of one.

One-dimensional solutions were found analytically and were simulated using MATLAB software. We set the *pdepe* function for non-negative solutions, and used otherwise standard numeric settings (relative error tolerance $10^{-3}$, absolute error tolerance $10^{-6}$), unless otherwise specified. The values used are shown in Table S4.

Two-dimensional simulations using the COMSOL software package were carried out with a relative error tolerance of $10^{-7}$. For both one- and two-dimensional models, we assumed homogeneous and isotropic auxin diffusion throughout the cytoplasm and apoplastic space. This is an approximation, as the presence of cellular compartments can slow down diffusion by about 4-fold (Sbalzarini et al., 2005), and the presence of cytoplasmic streaming can increase the effective transport rate. Degradation of auxin was assumed to be homogeneous throughout the cytoplasm (or part of it in regime 3). The key parameter grouping of the model under these assumptions is the rescaled characteristic length scale of degradation $\lambda/L$, whose estimated values are presented in the Table S1.

*Arabodpisis* and maize FG lengths were measured from pictures using ImageJ software. The distribution of FG lengths is shown in Fig. S7.

In order to assess the width of the cytoplasmic isthmus, we analyzed *Arabidopsis* wild-type (L*er*) plants expressing a membrane-localized GFP under the control of an FG-specific promoter (*pAtD123::EGFP-AtROP6C*, Escobar-Restrepo et al., 2007). As shown in Fig. S8, the width of the isthmus is in the order of 1 μm.

**Estimation of the membrane permeability parametes.**

We estimated auxin flux parameters from the data of Geisler et al. (2005). We assumed the following:

1. Linear dependence of the auxin trans-membrane flux on auxin concentration. This assumption can be justified by the fact that the auxin concentration applied in the experiment (500 nM) is lower than the known Km for the auxin transporters (more than 840 nM; Yang et al., 2006; Swarup et al., 2008).
2. Fast diffusion rate compared to transport. The data suggests that the assumption holds because the characteristic diffusion time (the ratio of the diffusion coefficient to the protoplast radius) is around $6 \cdot 10^{-5}$ m/s, with diffusion coefficient of $6 \cdot 10^{-10}$ $m^2/s$ (Grieneisen et al, 2007), while the estimated transmembrane flux values are slower than $10^{-8}$ m/s.
3. Background auxin in- and efflux are mediated by the protonated form only.
4. The effect of vacuolar trapping is insignificant.
5. Auxin flux in wild-type protoplasts kept in the dark does not involve any auxin transporter proteins.

6. PGP1 activity in mesophyll protoplasts is the same as in the FG.
7. As no auxin efflux carriers except for PGP1 are expressed in the FG, similarly to the *pgp19* mutant, we used the estimate of the transport rate in *pgp19* mutant protoplasts for further simulations of the wild-type FG.

Based on these assumptions we made the following estimations: the auxin efflux rate in the *pgp19* mutant is $1.1 \cdot 10^{-8}$ m/s; net passive auxin efflux (wild-type protoplasts in darkness) $5.6 \cdot 10^{-9}$ m/s; net passive auxin influx $4.3 \cdot 10^{-8}$ m/s; and the permeability of the membrane to the protonated form of auxin $1.3 \cdot 10^{-6}$ m/s.

Note that the parameter values for passive auxin flux, estimated based on the data by Geisler et al. (2005), indicate a lower membrane permeability in *Arabidopsis* protoplasts compared to the one estimated earlier by Gutknecht and Walter (1980) for lecitine bilayer membranes. However, we used the former, as they are obtained in a biological, and thus more relevant system for our studies.

***Geometrical features of the two-dimensional model***

For this model, we assumed that key properties of the FG can be described by the following geometry:

1. The shape of the FG is approximated by an ellipsoid.
2. The large central vacuole is represented by an intersection of an ellipsoid whose both semiradii are less than the semiradii of the FG by the value of $\Delta y$ and a shpere of radius 1/3.
3. The apoplast is modeled as a space between the plasma membrane of the FG and another membrane located at distance of $\Delta w$ from it, representing the plasma membranes of surrounding sporophytic cells.
4. The influx of auxin occurs in the micropylar pole of the plasma membrane of a surrounding cell.
5. The concentration of protonated auxin at the plasma membrane of cells located at the chalazal half of the FG is set to zero.

The geometry is thus axi-symmetrical two-dimensional. The values of the geometric parameters are presented in the Table S5.

### *Antagonistic auxin fluxes occur during polarization of germ lineage cells*

The auxin efflux carrier ZmPIN1a of maize was expressed as YFP fusion protein under control of the endogenous promoter (Gallavotti et al., 2008) to study the auxin flux occurring during ovule and germline development. As shown in Fig. 7M of the main text and in Fig. S2A,B, auxin flux as indicated by the polar localization of ZmPIN1a is directed at the tip of the ovule primordium towards the micropylar pole of the primordial germ cell (PGC) and megaspore cell (MSC), but is removed from the chalazal pole towards the ovule axis. After meiosis, ZmPIN1a localization at the micropylar pole starts to disappear, becoming very weak already at stage FG2/3 (Fig. S2C,D). In contrast, expression increased at the chalazal pole, presumably directing auxin towards the axis of the developing ovule and removing it from the chalazal pole of the developing FG. Strong ZmPIN1a-YFP signals were observed in nucellus cells surrounding the chalazal pole of the FG at stage FG5 (Fig. 7N of main text and Fig. S2E,F), when cellularization and separation of gametic and accessory cells occurs. During proliferation of antipodal cells, ZmPIN1a-YFP signals were also detectable inside these cells (Fig. 7O of main text and Fig. S2G,H) and appeared to accumulate in endosomes of antipodal cells within fully mature FGs (Fig. S2I,J). Whether auxin was removed from the chalazal pole of the maturing central cell could not be definitely determined, but as shown by *DR5* promoter activity, the highest auxin response was observed in the antipodal cell most distant from the central cell (Fig. 7K of main text and Fig. S13D), indicating that auxin flux is likely kept low in the immediate surrounding of the central cell.

## Sensitivity analysis

***Independent parameter groups taken into analysis.*** The mathematical model under regime 4 contains 12 linearly independent non-dimensional groupings.

1. Cytoplasmic isthmus width $\Delta y_{cyt}$ (Table S5)
2. Apoplast isthmus width $\Delta y_{apo}$ (Table S5)
3. Vacuole length $r_{vac}$ (Table S5)

4. Width *B* of the FG (Table S5)

5. Characteristic degradation rate (regarded as a ratio between the degradation velocity $\hat{q}_a := \hat{a} \cdot L$ and the diffusion velocity $\hat{q}_D := \frac{D}{L}$, and equivalent to the inverse of squared rescaled characteristic degradation length scale)

$$a = \frac{\hat{q}_a}{\hat{q}_D} = \hat{a} \cdot \frac{L^2}{D} = \left(\frac{\lambda}{L}\right)^{-2}$$

6. Rescaled active efflux rate of auxin from the cytoplasm to apoplast:

$$q_{c-a} = \frac{\hat{q}_{c-a}}{\hat{q}_D}$$

7. Characteristic dissociation velocity of auxin: $\beta := \frac{\hat{\beta}}{\hat{a}}$

8. Rescaled passive flux rate for protonized auxin: $q_{IAAH} = \frac{\hat{q}_{IAAH}}{\hat{q}_D}$

9. pKd of auxin

10. pH of the vacuole

11. pH of the cytoplasm

12. pH of the apoplast

The rate parameters here are normalized with respect to the characteristic diffusion velocity ($\hat{q}_D = \frac{D}{L}$), while the geometrical parameters are normalized with respect to the FG length *L*. *D* represents diffusion rate, the FG length *L*, and $\hat{a}$ is degradation rate in natural dimensions.

Alternatively, given fast auxin dissociation, six parameters influencing auxin flux (7—12) can be collected into three following parameters:

7.a. Rescaled influx from the apoplast to the cytoplasm $q_{a—c}$;

8.a. Rescaled efflux from the vacuole to the cytoplasm $q_{v—c}$;

9.a. Rescaled influx from the cytoplasm to the vacuole $q_{c—v.}$

***Calculation of the sensitivity.*** The robustness and sensitivity of the morphogen gradient can be addressed by studying how the perceived threshold concentration ($x_{thr}$) is shifted upon the perturbation in the parameter values ($\alpha$). Namely, we are interested in the fixed (threshold) level of the morphogen concentration at the physiological parameter value ($\alpha_0$) (de Lachapelle and Bergmann 2010). The sensitivity of the solution to deviation in the parameter values ($\alpha$) can be estimated from the full derivative formula:

$$\frac{\mathrm{d}u}{\mathrm{d}x} = \frac{\partial u}{\partial x}\cdot\frac{\mathrm{d}x}{\mathrm{d}x} + \frac{\partial u}{\partial \alpha}\cdot\frac{\mathrm{d}\alpha}{\mathrm{d}x} + o\left(\frac{1}{2}\cdot\frac{\partial^2 u}{\partial x^2} + \frac{1}{2}\cdot\frac{\partial^2 u}{\partial \alpha^2}\cdot\left(\frac{\mathrm{d}\alpha}{\mathrm{d}x}\right)^2\right) \qquad (*)$$

We are interested in the effects of finitesimally small shifts in the values of d$u$, d$x$, and d$\alpha$ which according to (*) are approximately related as follows:

$$\mathrm{d}u \approx \frac{\partial u}{\partial x}\cdot \mathrm{d}x + \frac{\partial u}{\partial \alpha}\cdot \mathrm{d}\alpha$$

At this stage we can address the *sensitivity of the concentration to the changes in the parameter values*, i.e. how the concentration in some point $x_0$ (d$x$ = 0) will be shifted upon perturbation d$\alpha$ (Fig. S9). Dividing both sides by $u_0$ we obtain:

$$\frac{\mathrm{d}u}{u_0} \approx \left.\frac{\partial \ln u}{\partial \ln \alpha}\right|_{\alpha_0, u_0}\cdot\frac{\mathrm{d}\alpha}{\alpha_0} \equiv \varepsilon_{u\alpha}\cdot\frac{\mathrm{d}\alpha}{\alpha_0}$$

Where $\varepsilon_{u\alpha}$ is the coefficient of sensitivity of concentration to the parameter values.

Then, we can question the *sensitivity of the threshold position to the concentration*, i.e. how the position of the threshold concentration will move if the concetration is changed under the fixed parameter values:

$$dx \approx \left(\frac{\partial \ln u}{\partial x}\Big|_{u_0,x_0}\right)^{-1} \cdot \frac{du}{u_0} \equiv \varepsilon_{ux} \cdot \frac{du}{u_0}$$

Where $\varepsilon_{ux}$ is the coefficient of sensitivtiy of the threshold position to the concentration. One can notice that it is given by the concentration value divided by the gradient at a given point:

$$\varepsilon_{ux} = u_0 \,/\, \frac{\partial u}{\partial x}\Big|_{x_0}$$

Further, we can study the *sensitivity of the threshold position to the perturbation in the parameter value*, i.e. how some position at which concentration is equal to some threshold concentration $u_0$ ($du = 0$) will shift upon perturbation in the parameter vale $d\alpha$:

$$dx \approx \left(\frac{\partial \ln u}{\partial x}\Big|_{u_0,x_0}\right)^{-1} \cdot \frac{\partial \ln u}{\partial \ln \alpha}\Big|_{\alpha_0,u_0} \cdot \frac{d\alpha}{\alpha_0} \equiv \varepsilon \cdot \frac{d\alpha}{\alpha_0}$$

Where $\varepsilon = \varepsilon_{ux} \cdot \varepsilon_{u\alpha}$. Particularly, as the partial differential equation under consideration is linear, the sensitivity of the concentration to the source intensity (the concentration of auxin at the micropylar pole) is equal to one ($\varepsilon_{u\alpha} = 1$), i.e. the sensitivity of the threshold position to the perturbation in the source is equivalent to the sensitivity to the perturbation in concentration.

***The sensitivity of the concentration to changes in the parameter values***. The concentration is highly sensitive to the changes in the pH of the apoplast and the source (i.e. auxin concentration in the neighbouring cells at the micropylar pole). Perturbations in these former parameters will be amplified by about 10 times. The perturbation in the rest of the parameters will be dampened, however (Table S2).

***The sensitivity of the threshold position to the concentration change.*** The threshold position could not be correctly distinguished in the micropylar part (i.e. it is shifted out of the FG) if the perturbation in the auxin concentration exceeds around 1%. With perturbations higher than 3.5%, the threshold determination becomes impossible also in the chalazal part (see Fig. 5 in the main text).

***The sensitivity of the threshold position to the perturbation in the parameter value*** can be found as the product of the two previously mentioned sensitivity coefficient.

## REFERENCES


**Abbruzzetti, S., Grandi, E., Viappiani, C., Bologna, S., Campanini, B., Raboni, S., Bettati, S. and Mozzarelli, A.** (2005). Kinetics of acid-induced spectral changes in the GFPmut2 chromophore. *J. Am. Chem. Soc.* **127**, 626–635.

**Chavarría-Krauser, A. and Ptashnyk, M.** (2010). Homogenization of long-range auxin transport in plant tissues. *Nonlinear Anal. Real World Appl.* **11**, 4524–4532.

**Escobar-Restrepo, J.-M., Huck, N., Kessler, S., Gagliardini, V., Gheyselinck, J., Yang, W.-C. and Grossniklaus, U.** (2007). The FERONIA receptor-like kinase mediates male-female interactions during pollen tube reception. *Science*. **317**, 656–660.

**Gallavotti, A., Yang, Y., Schmidt, R. J. and Jackson, D.** (2008). The relationship between auxin transport and maize branching. *Plant Physiol.* **147**, 1913–1923.

**Grieneisen, V. A., Xu, J., Maree, A. F. M., Hogeweg, P. and Scheres, B.** (2007). Auxin transport is sufficient to generate a maximum and gradient guiding root growth. *Nature* **449**, 1008–1013.

**Gutknecht, J. and Walter, A.** (1980). Transport of auxin (indoleacetic acid) through lipid bilayer membranes. *J. Membr. Biol.* **56**, 65–72.

**Liu, J., Mehdi, S., Topping, J., Tarkowski, P. and Lindsey, K.** (2010). Modelling and experimental analysis of hormonal crosstalk in *Arabidopsis*. *Mol. Syst. Biol.* **6**.

**Ljung, K., Ostin, A., Lioussanne, L. and Sandberg, G.** (2001). Developmental regulation of indole-3-acetic acid turnover in Scots pine seedlings. *Plant Physiol.* **125**, 464–475.

**Mravec, J., Kubes, M., Bielach, A., Gaykova, V., Petrásek, J., Skůpa, P., Chand, S., Benková, E., Zazímalová, E. and Friml, J.** (2008). Interaction of PIN and PGP transport mechanisms in auxin distribution-dependent development. *Development* **135**, 3345–3354.

**Rapparini, F., Tam, Y. Y. Y., Cohen, J. D. and Slovin, J. P.** (2002). Indole-3-acetic acid metabolism in *Lemna gibba* undergoes dynamic changes in response to growth temperature. *Plant Physiology* **128**, 1410–1416.

**Sequeira, L. and Mineo, L.** (1966). Partial purification and kinetics of indoleacetic acid oxidase from tobacco roots. *Plant physiology* **41**, 1200–1208.

**Slifkin, M.** (1984). Protonation rate constants of proline. *J. Mol. Liq.* **29**, 75–80.**Slifkin, M. A. and Ali, S. M.** (1991). Thermodynamic and rate parameters for alanine protonation reactions. *J. Chem. Soc., Faraday Trans.* **87**, 3241–3243.

# SUPPLEMENTARY TABLES

**Table S1. Values of degradation rate and corresponding gradient steepness at regime 1**

| Ref. | Object | Degradation rate, $\hat{a}$ | Half-life | $a$ | $\lambda/L$ | GS |
|---|---|---|---|---|---|---|
| (Sequeira and Mineo,1966) | Tobacco leaf protoplasts | $5\cdot10^{-4}$ | 23 min | $4.08\cdot10^{-3}$ | 15.6 | 0.204% |
| (Ljung et al., 2001) | Scots pine seedlings | $2.67\cdot10^{-5}$ | 7.2 h | $2.18\cdot10^{-4}$ | 67.7 | 0.0109% |
| (Rapparini et al., 2002) | *Lemna gibba* (aquatic monocot) | $<1.93\cdot10^{-3}$ | <6 min | $1.58\cdot10^{-2}$ | 7.97 | 0.783% |
| (Grieneisen et al.,2007) | Model fitting | $5\cdot10^{-6}$ | 3.85 h | $4.08\cdot10^{-5}$ | 156 | 0.00204% |
| (Liu et al., 2010) | Model fitting | 2 | 0.35 s | $1.63\cdot10^{1}$ | 0.247 | 96.49% |

**Table S2. Sensitivity of the model to perturbation in parameters (regime 4 in two dimensions). For description of parameters see Table 2 and 3.**

| Parameter | median of $\|\varepsilon\|$ | maximum of $\|\varepsilon\|$ |
|---|---|---|
| $\Delta y$ | $2.66 \cdot 10^{-2}$ | $3.98 \cdot 10^{-2}$ |
| $w$ | $1.15 \cdot 10^{-2}$ | $1.91 \cdot 10^{-2}$ |
| $B$ | $4.85 \cdot 10^{-5}$ | $6.56 \cdot 10^{-5}$ |
| $r_{\mathrm{vac}}$ | $8.79 \cdot 10^{-4}$ | $4.91 \cdot 10^{-3}$ |
| $s$ | $1.67 \cdot 10^{-2}$ | $2.94 \cdot 10^{-2}$ |
| $D$ | $6.57 \cdot 10^{-3}$ | $9.78 \cdot 10^{-3}$ |
| $k_{\mathrm{AUX1}}^{\mathrm{micr}}$ | $2.00 \cdot 10^{-2}$ | $2.98 \cdot 10^{-2}$ |
| $q_{c\text{-a}}$ | $6.08 \cdot 10^{-5}$ | $7.24 \cdot 10^{-5}$ |
| $q_{\mathrm{a\text{-}c}}$ | $1.50 \cdot 10^{-2}$ | $2.26 \cdot 10^{-2}$ |
| $q_{\mathrm{c\text{-}v}}$ | $2.62 \cdot 10^{-4}$ | $2.85 \cdot 10^{-4}$ |
| $q_{\mathrm{v\text{-}c}}$ | $7.50 \cdot 10^{-4}$ | $1.94 \cdot 10^{-3}$ |
| $p_{\mathrm{IAA}}$ | $1.50 \cdot 10^{-2}$ | $2.26 \cdot 10^{-2}$ |
| $K$ | $1.40 \cdot 10^{-3}$ | $2.34 \cdot 10^{-3}$ |
| $\mathrm{pH}_{\mathrm{apo}}$ | $1.36 \cdot 10^{-3}$ | $2.31 \cdot 10^{-3}$ |
| $\mathrm{pH}_{\mathrm{cyt}}$ | $2.41 \cdot 10^{-3}$ | $2.65 \cdot 10^{-3}$ |
| $\mathrm{pH}_{\mathrm{vac}}$ | $1.21 \cdot 10^{-2}$ | $3.11 \cdot 10^{-2}$ |

**Table S3. The *p*-value of the one-sided Wilcoxon signed rank test with the alternative hypothesis that the $\log_2$ fluorescence ratios in the ovules of the degron plants (pUBQ10:degron-GFP) are higher than in ovules of the control plants (pUBQ10:degron-GFP).**

| Stage | $\log_2$[ ES / integument ] | $\log_2$[ ES / nucellus ] | $\log_2$[integument / nucellus] |
|---|---|---|---|
| FM | 0.1397 | 0.0005 * | 0.0026 * |
| FG3 | 0.7665 | 0.1409 | 0.0033 * |

* significant within 0.05 confidence interval

**Table S4. Reaction, diffusion and transport parameters**

| Abbreviation | Parameter | Value | Reference |
|---|---|---|---|
| $a$ | dimensionless degradation rate | 0.0158 | |
| $\lambda/L$ | rescaled characteristic length scale | $a^{-1/2} = 7.97$ | |
| $\beta$ | dimensionless protonation rate | $8.33 \cdot 10^4$ | |
| $pH_{apo}$ | apoplastic pH | 5.00 | |
| $pH_{cyt}$ | cytoplasmatic $pH$ | 7.60 | (Chavarría-Krauser and Ptashnyk, 2010) |
| $pK_d$ | IAA dissociation constant | 4.75 | (Chavarría-Krauser and Ptashnyk, 2010) |
| $k_d$ | dissociation rate (estimation for auxin) | 1.4·106 s-1 | (Chavarría-Krauser and Ptashnyk, 2010) |
| $P_{[HA]}$ | permeability to non-ionized auxin | $4.8 \cdot 10^{-6}$ m/s | (Geisler et al., 2005) |
| $P_{[A-]}$ | permeability to ionized auxin | $<10^{-11}$ m/s | (Gutknecht and Walter, 1980) |
| $q_1$ | dimensionless membrane permeability to IAAH | 5.50 | |
| $q_2$ | dimensionless membrane permeability to $IAA^-$ | $1.67 \cdot 10^{-6}$ | |
| $v_1$ | dimensionless IAAH diffusion coefficient in the membrane | $q_1 \times \Delta x = P_1 \Delta \hat{x}/D$ | |
| $v_2$ | dimensionless $IAA^-$ diffusion coefficient in the membrane | $q_2 \times \Delta x$ | |

| | | | |
|---|---|---|---|
| $b^{ES}_{IAA}$ | auxin production rate in the ES (NCAS model) | {0,2,3} | |
| $b^{adj.c.}_{IAA}$ | auxin production rate in the adjacent cells (NCAS model) | 0.189 | |
| $c_{thr}$ | threshold of [IAA] for NCAS promoter activation | 0.189 | |
| $b^{adj.c.}_{NCAS}$ | NCAS production rate in the adjacent cells | 5 | |
| $a_{NCAS}$ | NCAS degratation rate in the cytoplasm | 30 | |
| $D_{NCAS}$ | NCAS diffusion coefficient | 0.05 | |

**Table S5: Geometric parameter values**

| Abbrev. | Value | Description |
|---|---|---|
| $L$ | 70 μm | *A. thaliana* FG length at FG5 stage |
| $\Delta\hat{x}$ | 5 nm | membrane width |
| $\Delta x$ | $\Delta\hat{x}/L$ | dimensionless membrane width |
| $\Delta\hat{y}$ | 1 μm | width of cytoplasmic path around the vacuole |
| $\Delta y$ | $\Delta\hat{y}/L$ | dimensionless width of cytoplasmic path around the vacuole |
| $\hat{w}$ | 50 nm | the width of the apoplast |
| $w$ | $\hat{w}/L$ | rescaled width of the apoplast |
| $s$ | $L/10$ | the localization of the sporophytic cells providing the source of auxin |
| $B$ | 2/5 $L$ | FG width-to-length ratio |
| $r_{vac}$ | 2/3 $L$ | vacuole length |

## FIGURES

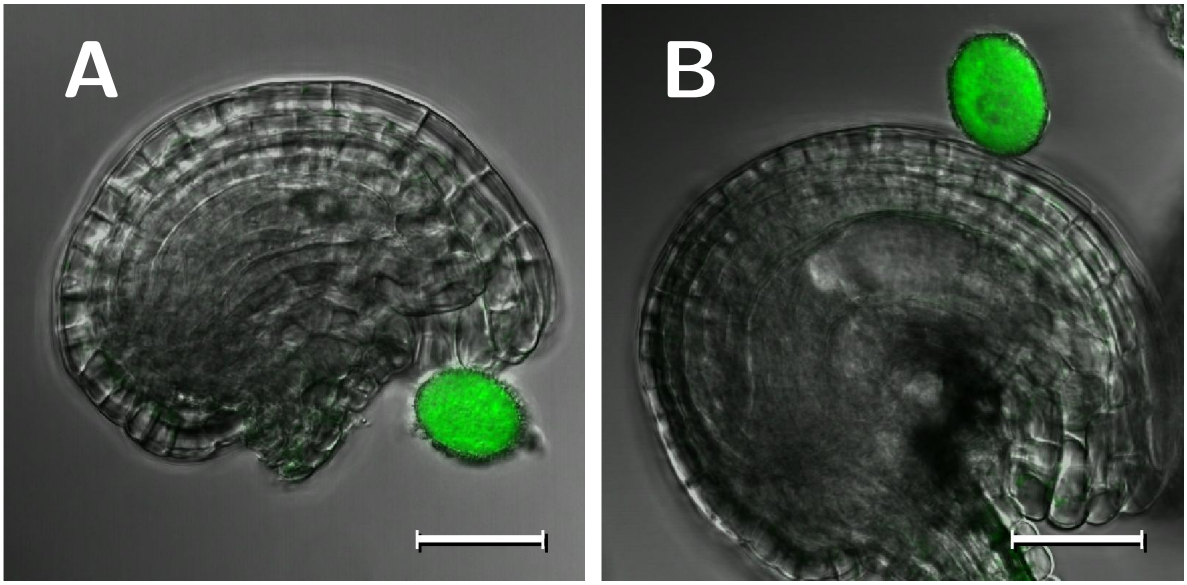


**Fig. S1. PIN8 protein is not detected in the *Arabidopsis* ovules.** Ovules and pollen from plants carrying PIN8::PIN8:GFP promoter-fusion construct were analysed. While a PIN8:GFP signal is clearly observed in the pollen grains as expected, no signal can be detected in ovules during FG4 (**A**) and FG6 (**B**) stages. Scale bars: 30 μm.

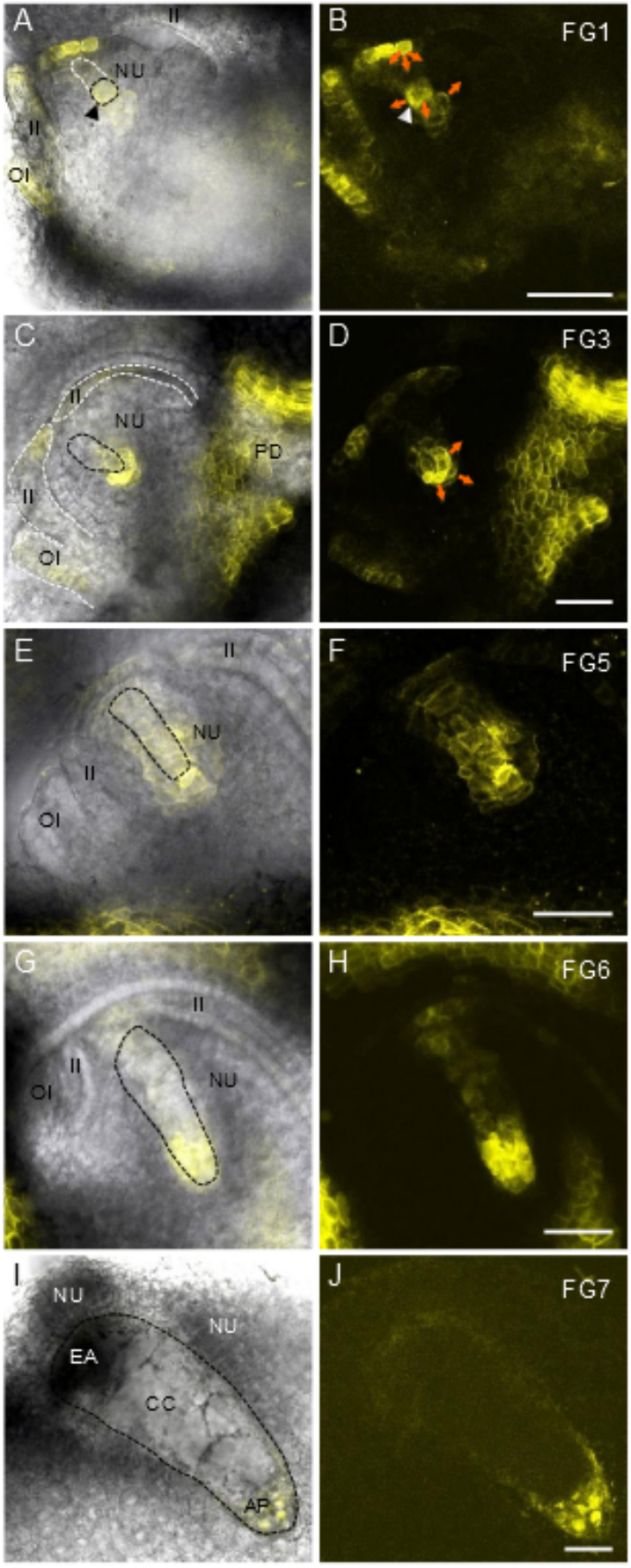
A
II
NU
II
OI
B
FG1
C
II
NU
PD
II
OI
D
FG3
E
II
NU
II
OI
F
FG5
G
II
II
OI
NU
H
FG6
I
NU
NU
EA
CC
AP
J
FG7

**Fig. S2 *(preceding page)*. Localization of the auxin efflux carrier ZmPIN1a during ovule development in maize.** ZmPIN1a was expressed as a YFP fusion protein under control of its endogenous promoter. Orange arrows indicate the predicted auxin flux according to polarized ZmPIN1a localization. (**A**) A female gametophyte at stage FG1 (shortly after meiosis): ZmPIN1a-YFP is localized at the plasma membrane of micropylar nucellus cells pointing towards the degenerating megaspores (encircled by a white dashed line) as well as around the functional megaspore (indicated by a black dashed line and arrowhead). Additionally, ZmPIN1a-YFP is visible in the developing integuments. (**B**) Fluorescence image of (A). The arrowhead points towards the position of the functional megaspore. (**C**) Stage FG3: ZmPIN1a-YFP is no longer detectable at micropylar nucellus cells. YFP signals in nucellus cells, surrounding the chalazal pole of the female gametophyte, have increased in intensity. Additionally, ZmPIN1a-YFP is visible in the integuments and strongly in the pedicel cells differentiating vascular tissue. Note that the pericarp was removed. (**D**) Fluorescence image of (C). (**E**) Stage FG5: ZmPIN1a-YFP signals are strongest in nucellus cells surrounding the chalazal pole of the female gametophyte. (**F**) Fluorescence image of (E). (**G**) Stage FG6: ZmPIN1a-YFP signals are strongest in nucellus cells surrounding and inside antipodal cells. (H) Fluorescence image of (G). (**I**) Mature stage FG7: Integuments were removed. ZmPIN1a-YFP signals inside antipodal cells seem to be mainly localized to the endosomal compartment. (**J**) Fluorescence image of (I). (A, C, E, G and I) merged bright field and fluorescence images. The female gametophyte is indicated by a black dashed line. Abbreviations: AP: antipodal cells, CC: central cell, EA: egg apparatus, II: inner integument, NU: nucellus, OI: outer integument, PD: pedicel. Scale bars: 50 μm.

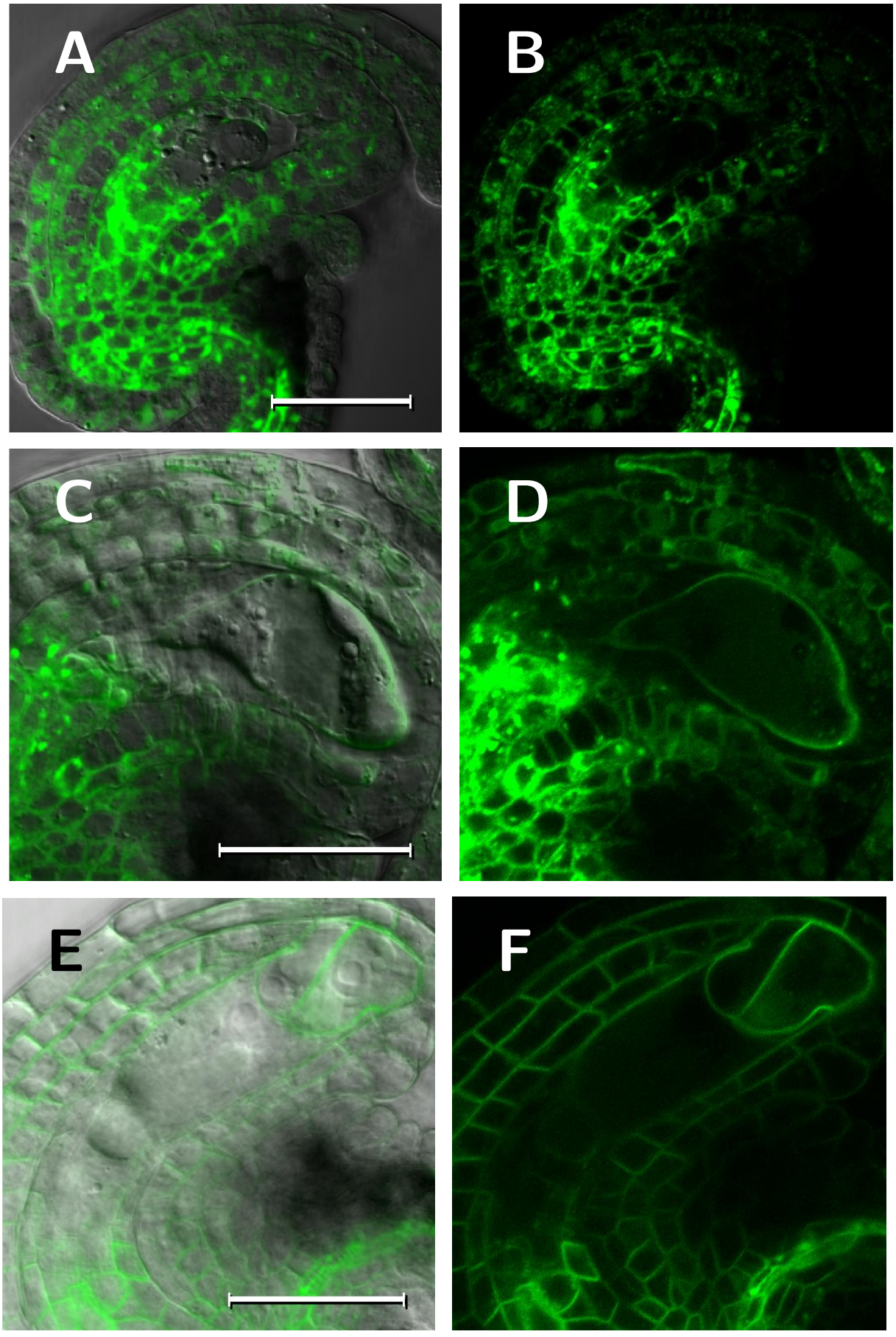
A
B
C
D
E
F

**Fig. S3 *(preceding page)*. PGP1 is expressed and evenly distributed over the plasma membrane in the *Arabidopsis* female gametophyte.** ( **A, B**) FG3 stage: PGP1:GFP is highly expressed in the sporophytic tissue in the chalazal part of the nucellus, a moderate signal is also observed within the two-nucleate FG, ( **C, D**) FG4 stage: the strong PGP1:GFP signal remains in the chalazal part of the nucellus; the almost uniform staining in the plasma membrane of the four-nucleate FG becomes more distinct; ( **E, F**) FG6 stage: strong PGP1:GFP expression can now be observed within the synergid (the cell on the right in the top right corner) and the egg cell (the cell on the left). (A, C, and E) Overlay of the DIC and GFP channels; (B, D, and F) corresponding GFP channel alone. The samples A, B, and C, D were plasmolysed and cleared with the 1M glycin solution to better visualize the localization in the FG membrane. Scale bars: 30 μm.

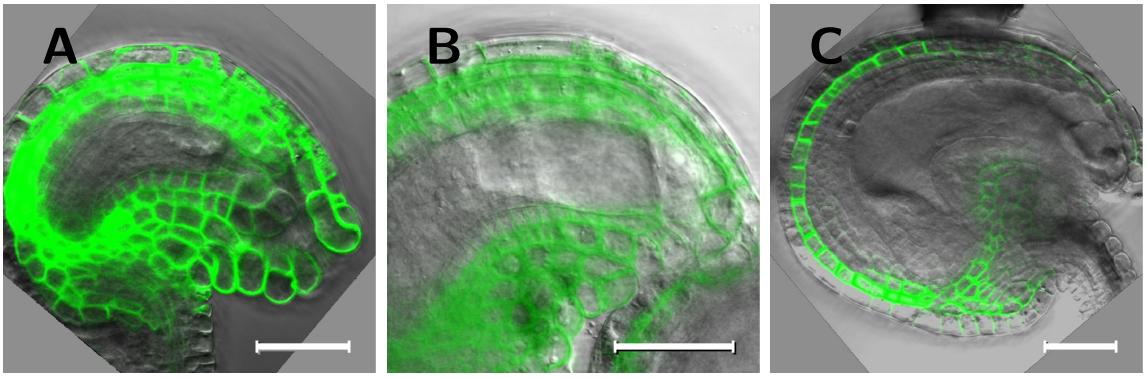


**Fig. S4. PGP19 is expressed in the sporophytic tissues of the *Arabidopsis* ovules.** (**A**) functional megaspore stage (FG1) and (**B**) FG6 stage: PGP19:GFP is expressed in the inner and outer integuments. (C) FG7 stage: PGP19:GFP is localized to the subepidermal cell layer only. Scale bars: 30 μm.

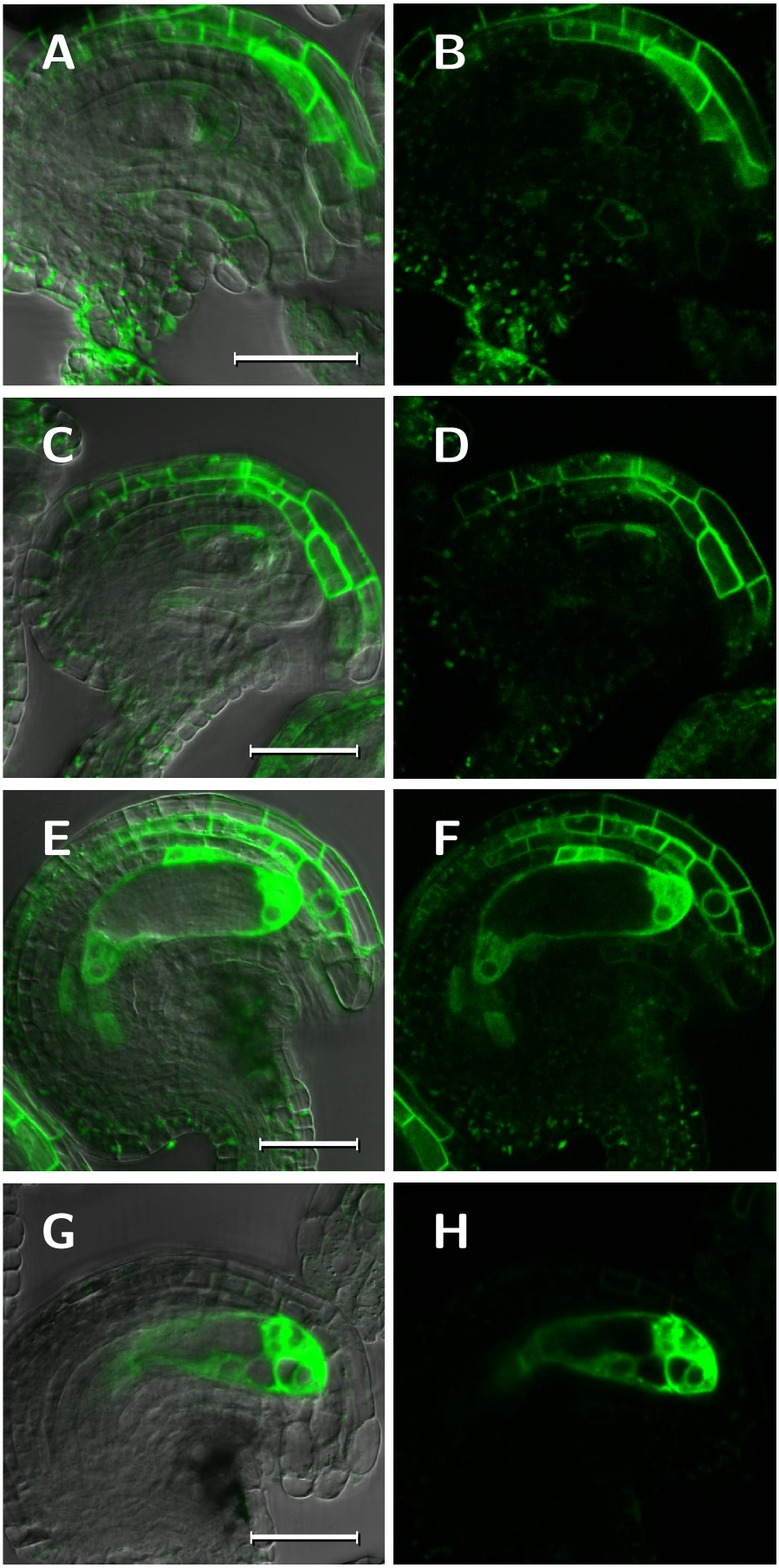
A
B
C
D
E
F
G
H

**Fig. S5 *(preceding page).* AUX1 is expressed and polarly distributed in the plasma membrane in the *Arabidopsis* female gametophyte from the FG4 stage onward.** (**A, B**) FG2 stage: AUX1:YFP is strongly expressed within the upper part of the outer integument and, at a lower extent, the sporophytic tissue of the nucellus. (**C, D**) FG3 stage: AUX1:YFP expression becomes stronger in the nucellus. (**E, F**) FG4 stage: AUX1:YFP expression appears within the FG first at the four-nulceate stage, with the YFP intensity in the micropylar compartment approximately 5 times higher than in the chalazal one; expression within the endothelium becomes stronger; some expression appears also in the chalazal part of the nucellus. (**G, H**) FG7 stage: AUX1:YFP expression becomes stongest in the cells of the FG, with signal in the surrounding tissues becoming undetectable. (A, C, E and G) Overlay of the DIC and GFP channels; (B, D, F and H) corresponding GFP channel alone. Scale bars: 30 μm.

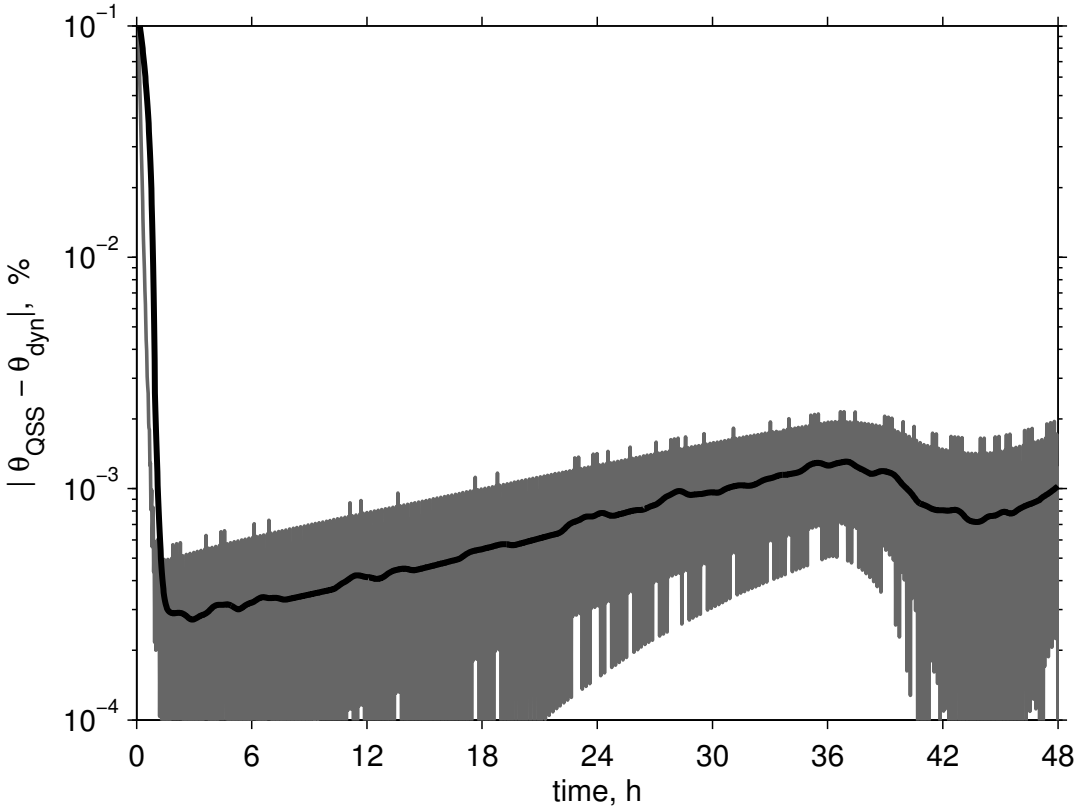


**Fig. S6. Numerical studies suggest that a quasi-steady state assumption about growth leads to a negligibly small error in regime 1.** The absolute value of difference between the gradient steepness found as quasi-steady state and dynamic solution $|\theta_{\mathrm{QSS}} - \theta_{\mathrm{dyn}}|$ expressed in percentage points. Note that the absolute value of the difference does not exceed 0.0022% after initial equilibration during the first 38 minutes. The original data (gray line) was smoothened with a moving average filter with window size of two hours (black line). The relative error tolerance of the ODE solver was set to $10^{-5}$.

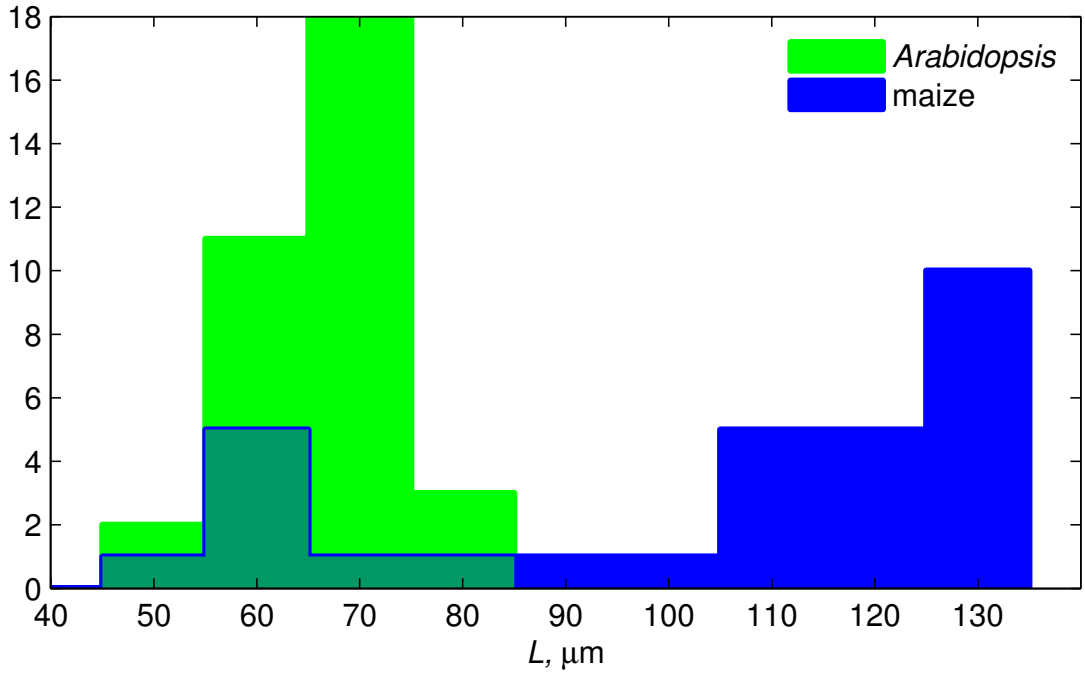


**Fig. S7. Distribution of the female gametophyte lengths in Arabidopsis and maize at stage FG4/5.** The graph shows the distribution of FG lengths (in µm) measured from micrographs. *Arabidopsis* is shown in green, maize in blue

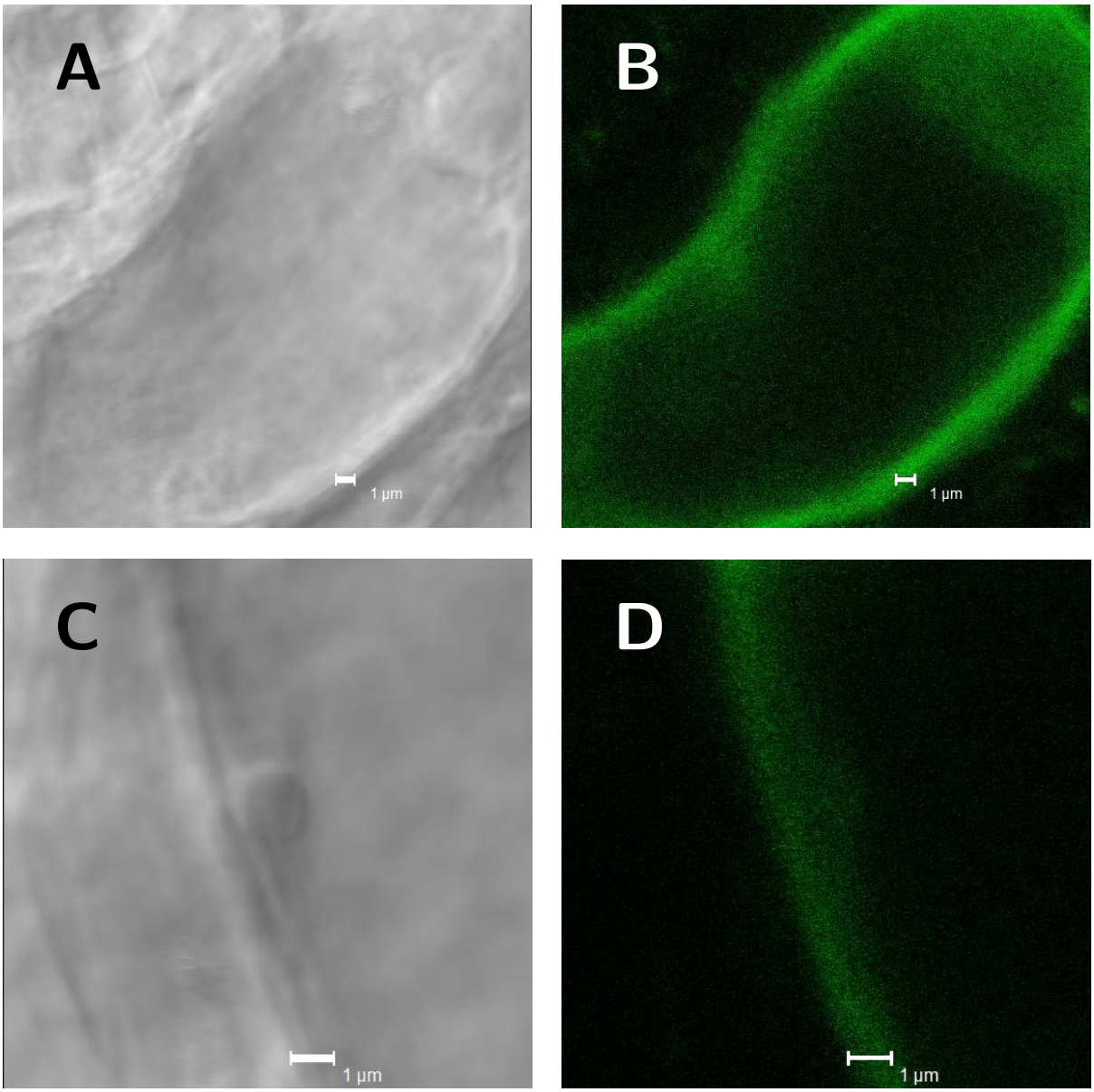


**Fig. S8. The isthmus between central vacoule and female gametophyte membranes.** (**A, C**) Differential interference contrast of *Arabidopsis* wild-type FG4 FGs. ( **B, D**). Fluorescent micrographs of the same ovules expressing a membrane-localized GFP driven by an FG-specific promoter. The isthmus is around 1 µm in width.

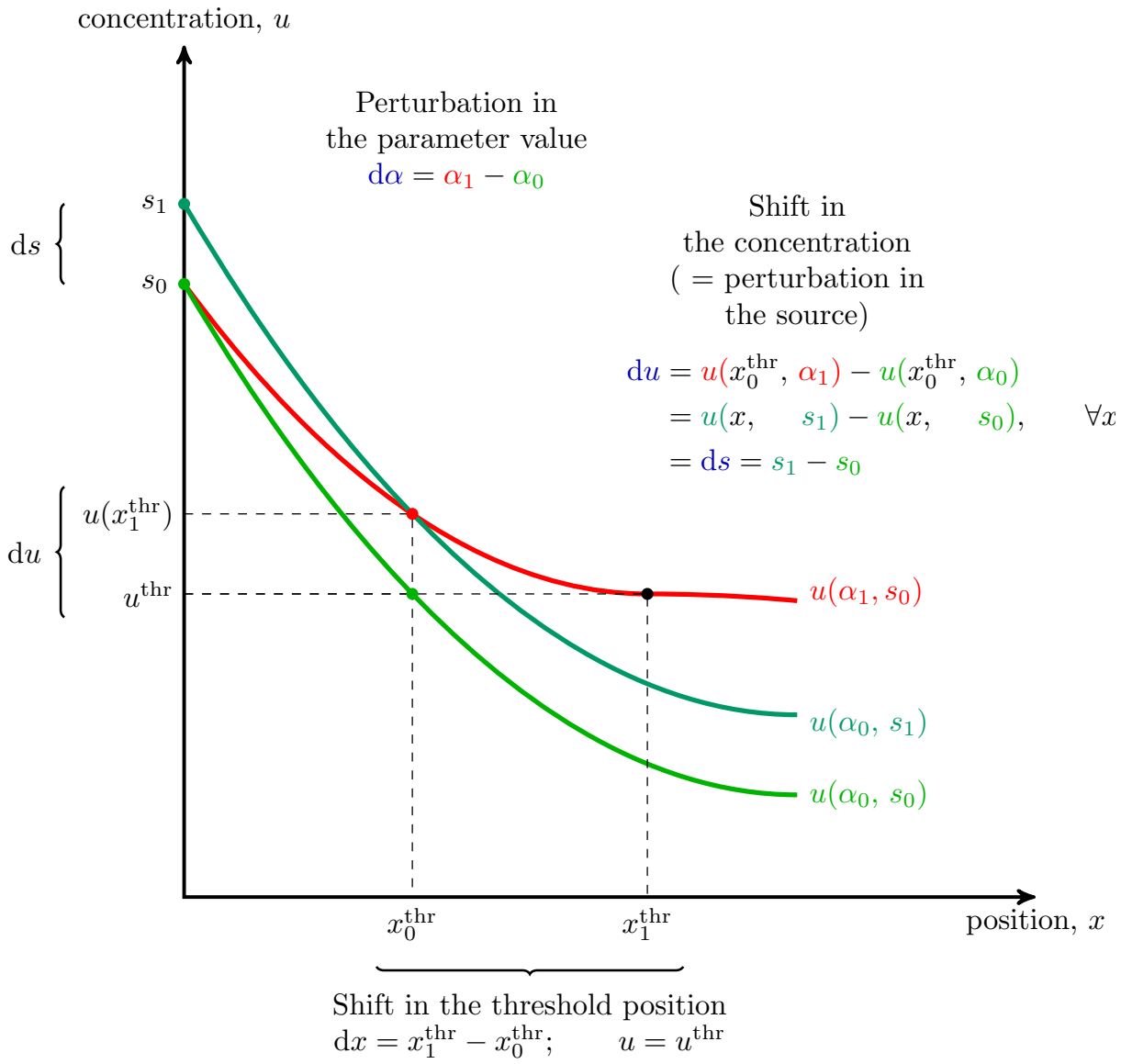


**Fig. S9. The principle of the sensitivity analysis.** The profile of the morphogen under physiological conditions is shown in green. We study the behavior of the threshold position ($x_0^{\mathrm{thr}}$), defined by the threshold concentration ($u^{\mathrm{thr}}$), upon perturbation in the parameter values. After perturbing parameter $\alpha$ by some small value $\mathrm{d}\alpha$, we obtain another, distorted profile (in red), where the threshold concentration ($u^{\mathrm{thr}}$) is pointing to another $x$-position, $x_1^{\mathrm{thr}}$. The concentration in the physiological threshold position is now shifted by $\mathrm{d}u$. Equivalently, the same value of concentration shift is achieved at all the x-positions if we perturb the source by $\mathrm{d}s = \mathrm{d}u$. The chain rule given in the supplementary text provides the connection between these shifts.

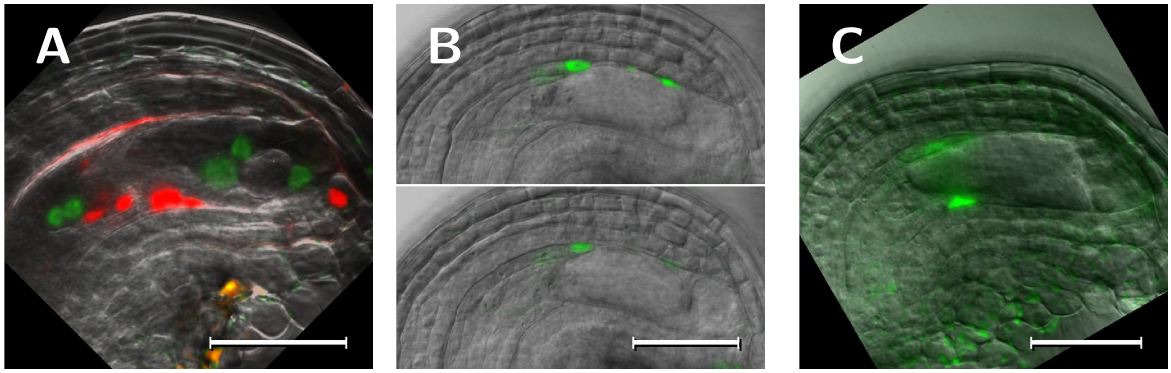


**Fig. S10. *DR5* activity at the FG5 and FG6 stage in *Arabidopsis* ovules is observed only in the sporophytic tissue** (**A**) At the FG5 stage, DR5::NLS:tdTomato expression in the ovule is localized to the nucellar cells on the lower (concave) side of the ovule along the whole length of the FG, with a stronger signal in the chalazal part; the gametic cell fate marker (green, AKV::H2B:YFP) shows no colocalization with the red DR5 signal. (**B**) Two $z$-sections of a FG at the FG5 stage are shown. DR5::SV40:3GFP is expressed in the endothelial cells adjacent to the chalazal pole of the FG. (**C**) DR5::GFP-ER expression in the FG5 stage: DR5 signal is observed in the endothelial cells surrounding the chalazal pole of the FG; the endothelial cells near the micropylar part have already degraded. Scale bars: 30 μm.

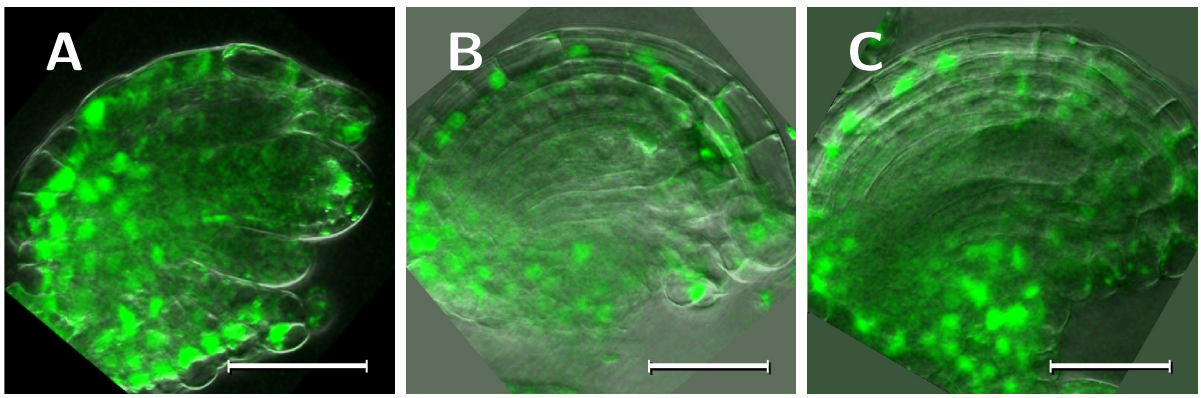


**Fig. S11. The 35S::DII-Venus sensor is expressed in the outer integument and the chalazal pole but not in the female gametophyte of the *Arabidopsis* ovules.** ( **A**) Functional megaspore stage: the DII-Venus fluorescence is strong in the chalaza of the ovule and in a micropylar-most nucellar cells. ( **B**) FG3 stage: the DII-Venus fluorescence appears in the outer integument. ( **C**). FG4 stage. Note, at no stage can the DII-Venus fluorescence be seen within the FG. Scale bars: 30 μm.

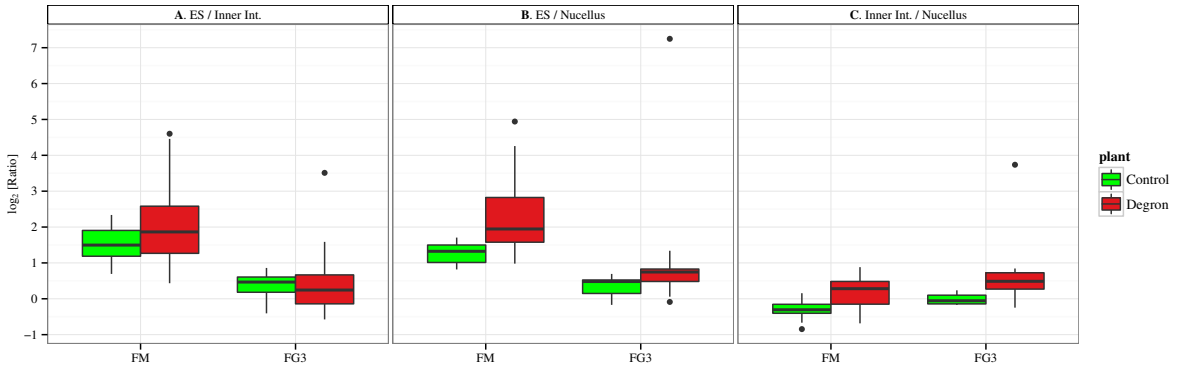


**Fig. S12. Quantification of the fluorescence in the pUBQ10::degron:GFP and the pUBQ10::GFP plants indicates that the pattern of the auxin activity in the ovules is consistent with the *DR5* expression.** Accounting for the non-uniform activity of the UBQ10 promoter driving the degron:GFP sensor construct, we performed intensity ratio measurements in the control pUBQ10::GFP and sensor pUBQ10::degron:GFP plants in order to infer the pattern of auxin distribution in the developing ovules. The GFP fluorescent images (grayscale, 12-bit) of the ovules from the degron (pUBQ10::degron:GFP) and the control (pUBQ10::GFP) transgenic lines were manually segmented and the median of the intensity was quantified using the ImageJ software. The intensity was measured for three regions (FG, endothelium surrounding the FG, and inner integument) from 2 degron lines and 6 control lines at stages the functional megaspore (FM) and late two-nucleate stage (FG3; all stages according to Christensen et al., 1997) ($n > 6$ per group). The $\log_2$-transformed ratios between the median intensity of the regions for each image were subjected to a one-sided Wilcoxon signed-rank test in R software (version 2.14.1). (**A**) The intensity ratio between the FG and the inner integument is insignificantly higher in the degron carrying plants at the FM stage and approximately the same at the FG3 stage, suggesting that the level of auxin is lower in the FG than in the inner integument at the FM stage and similar at the FG3 stage. (**B**) The intensity ratio between the FG and the nucellus is higher in the degron carrying plants at the functional megaspore (FM) stage (also referred to as FG1) and possibly lower at the FG3 stage, suggesting that the level of auxin is lower in the FG than in the nucellus at this stage and possibly lower at the FG3 stage. (**C**) In the degron plants, the fluorescence intensity ratio between the inner integument and the nucellus is significantly lower compared to the control at both FM and FG3 stage, which suggests that auxin activity in the inner integument is lower than in the nucellus. Significance levels: $^*$ –$p < 0.004$ (significant); $^\dagger$ $p < 0.15$ (insignificant trend).

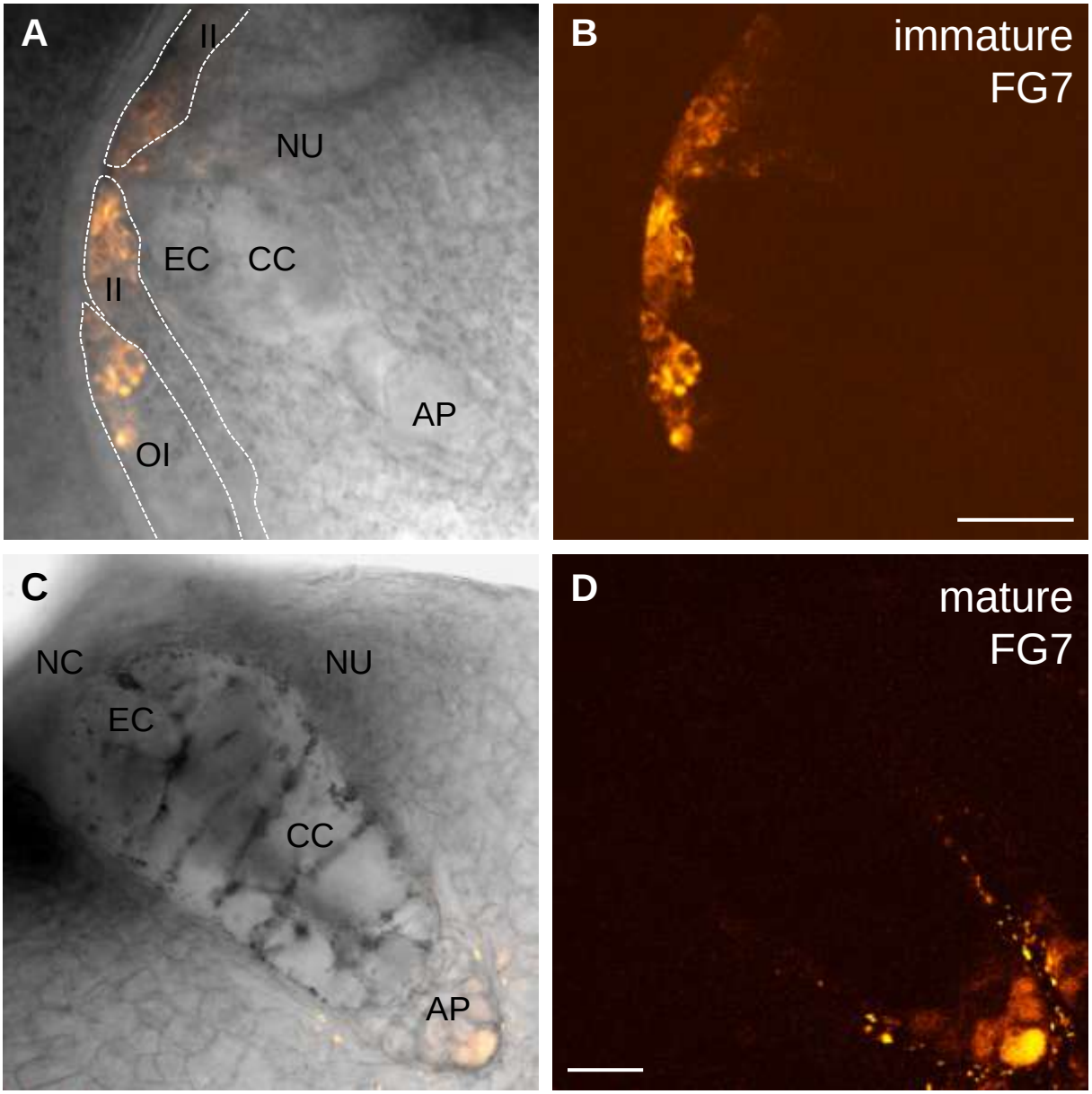


**Fig. S13. Auxin response in the micropylar tips of integuments and at the chalazal pole inside the mature female gametophyte of maize.** Auxin response is indirectly visualized by the activity of the synthetic *DR5* promoter driving ER localized mRFP marker protein expression. (**A**) Early FG at stage FG7. Antipodals start to proliferate. Strong mRFP signals signals are visible in the tips of the integuments (white dashed lines), but not in the micropylar nucellus cap. (**B**) Enhanced fluorescence image of (A) showing lack of mRFP signals inside the mature FG. (**C**) Mature FG. Integuments are removed. Strongest mRFP signal is visible in the antipodal cell most distant to the central cell. (**D**) Enhanced fluorescence image of (C) showing an mRFP gradient inside the antipodal cell cluster, with lowest signal in antipodal cells neighboring the central cell. (A and C) merged bright field and epifluorescent images. (B and D) Fluorescence images of (A) and (C), respectively. Abbreviations: AP: antipodal cells, CC: central cell, EC: egg cell, II: inner integument, NC: nucellar cap, NU: nucellus, OI: outer integument. Scale bars: 50 μm.

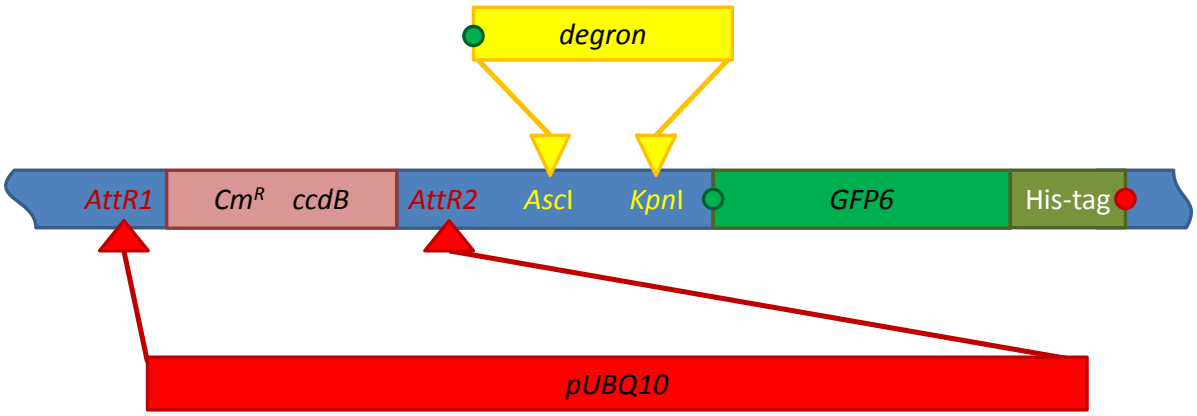


**Fig. S14. Scheme of cloning of the pUBQ10::degron:GFP plasmid.** The pUBQ10::degron:GFP plasmid was obtained in two steps. First, the pMDC111 (Curtis and Grossniklaus, 2003) destination vector was modified by inserting a sequence encoding the 6-amino acid long degron consensus core motif of domain II of AUX/IAA proteins, VGWPPV, between the AscI and KpnI restriction sites as a C-terminal in-frame fusion to GFP6-His-tag carried in the original vector. Subsequently, an entry clone carrying the 2.5 kb *Arabidopsis UBQ10* ubiquitin promoter was combined with the modified destination vector through a Gateway LR reaction.